# Reflectance Spectrum and Birefringence of the Retinal Nerve Fiber Layer With Hypertensive Damage of Axonal Cytoskeleton

Xiang-Run Huang, Robert W. Knighton, Ye Z. Spector, Jianzhong Qiao, Wei Kong, and Qi Zhao

Bascom Palmer Eye Institute, University of Miami Miller School of Medicine, Miami, Florida, United States

Correspondence: Xiang-Run Huang, Bascom Palmer Eye Institute, University of Miami Miller School of Medicine, 1638 NW Tenth Avenue, Miami, FL 33136, USA; xhuang3@med.miami.edu.

**PURPOSE.** Glaucoma damages the retinal nerve fiber layer (RNFL). This study used precise multimodal image registration to investigate the changes of the RNFL reflectance spectrum and birefringence in nerve fiber bundles with different degrees of axonal damage.

**METHODS.** The reflectance spectrum of individual nerve fiber bundles in normal rats and rats with experimental glaucoma was measured from 400 to 830 nm and their birefringence was measured at 500 nm. Optical measurements of the same bundles were made at different distances from the optic nerve head (ONH). After the optical measurements, the axonal cytoskeleton of the RNFL was evaluated by confocal microscopy to assess the severity of cytoskeletal change.

**RESULTS.** For normal bundles, the shape of the RNFL reflectance spectrum and the value of RNFL birefringence did not change along bundles. In treated retinas, damage to the cytoskeleton varied within and across retinas. The damage in retinal sectors was subjectively graded from normal-looking to severe. Change of spectral shape occurred near the ONH in all sectors studied. This change became more prominent and occurred farther from the ONH with increased damage severity. In contrast, RNFL birefringence did not show change in normal-looking sectors, but decreased in sectors with mild and moderate damage. The birefringence of severely damaged sectors was either within or below the normal range.

**CONCLUSIONS.** Varying degrees of cytoskeletal damage affect the RNFL reflectance spectrum and birefringence differently, supporting differences in the ultrastructural basis for the two optical properties. Both properties, however, may provide a means to detect disease and to estimate ultrastructural damage of the RNFL in glaucoma.

Keywords: retinal nerve fiber layer, reflectance spectrum, birefringence, glaucomatous damage, axonal cytoskeleton

The diagnosis and management of glaucoma require sensitive methods for detecting and measuring damage to retinal ganglion cells and their axons. Optical methods are commonly used to assess the retinal nerve fiber layer (RNFL), which lies just under the retinal surface and consists of the axons of retinal ganglion cells. These optical methods often rely on the optical properties of the RNFL: reflectance and birefringence. Considerable knowledge of RNFL optical properties in normal retinas has been gained, yet knowledge of how these optical properties change in diseased retinas is incomplete. This study aimed to extend our understanding of RNFL reflectance and birefringence in nerve fiber bundles with hypertensive damage.

The RNFL observed in a fundus image has long been used in clinic practice to assess loss of nerve fiber bundles in glaucoma.[1,2] The newer method of optical coherence tomography (OCT) uses macrostructural imaging of the retina to measure RNFL thickness.[3] Both methods rely on RNFL reflectance, which arises from light scattering by the ultrastructure of nerve fiber bundles.[4–7] Recent studies suggest that the reflectance property itself changes in early glaucoma, perhaps before thinning of the RNFL.[8–12]

Accurate quantitative understanding of the RNFL reflectance must account for the fact that it is highly directional with a geometry consistent with light scattering by cylinders.[4,7] Light scattered by a cylinder or an array of perfectly aligned cylinders is confined to a conical sheet coaxial with the cylinder axis. Misalignment of cylinders in a scattering array will broaden the scattered sheet and, in addition, the finite apertures of the light source and camera also spread the measured sheet. An evident example of directional reflectance of the RNFL appears in OCT cross-sectional images of the optic nerve head (ONH), where the RNFL reflectance decreases rapidly and bundles disappear as the bundles turn and enter the optic nerve. For bundles around the ONH, the directionality of RNFL reflectance can result in a 5:1 variation in relative reflectance measured by OCT that must be addressed in clinical applications.[13]

Another property of the RNFL that characterizes tissue ultrastructure is its reflectance spectrum. In normal retina, RNFL reflectance is wavelength dependent with reflectance high at visible wavelengths and lower at near infrared wavelengths.[7] A RNFL reflectance spectrum can be described by a two-mechanism scattering model, in which both thin and thick cylinders contribute to the reflectance, with thin cylinders contributing more at short wavelengths and thick cylinders dominating the reflectance at long wavelengths. We have shown earlier that the RNFL reflectance spectrum changes

in hypertensive retinas and the change is associated with axonal ultrastructural damage.[14] Hence, change of the RNFL reflectance spectrum in diseased retinas may provide an insight into ultrastructural change in the RNFL.

The RNFL exhibits form birefringence due to preferentially oriented ultrastructure.[6,15,16] Retinal nerve fiber layer birefringence ($\Delta n$) can be determined by measuring the retardance ($\delta$) of polarized light passing through the tissue; $\Delta n$ is then calculated as the ratio of $\delta$ and the tissue thickness ($T$). $\Delta n$ of the RNFL is an intrinsic property of the tissue. In normal human retinas, $\Delta n$ varies around the ONH but is approximately constant along bundles.[17-19]

The anatomic bases for the RNFL reflectance and birefringence are only partially known. In vitro and in vivo experiments show that $\delta$ decreases as microtubules (MTs) are depolymerized by colchicine.[20,21] In rodent retinas, MTs contribute at least 85% of $\delta$,[20] and electron microscopy shows that $\Delta n$ of the RNFL is associated with axonal MTs in primate retinas.[22] Microtubules are also found to contribute to the RNFL reflectance.[23,24] Different from the RNFL birefringence, however, in rodent retinas MTs contribute not more than 50% of the RNFL reflectance.[24] Other structures that may contribute to the RNFL reflectance have not yet been identified.

Glaucoma damages the ultrastructure of retinal ganglion cell axons.[25-34] Consequently, measurements of the RNFL reflectance spectra and birefringence should be able to detect early structural changes in glaucoma, changes that may precede irreversible damage. Because the anatomic bases for the RNFL reflectance and birefringence are not identical, changes of the RNFL reflectance spectrum and $\Delta n$ with the development of glaucoma may not be the same. In this study, we used isolated retinas from a rat model of glaucoma to study the RNFL reflectance and birefringence in retinal nerve fiber bundles with different degrees of ultrastructural damage.

## MATERIALS AND METHODS

### Rat Model of Glaucoma and Tissue Preparation

Female Wistar rats, approximately 6 months old and weighing 250 g, were used in this study. Animals were housed under a 12-hour light and 12-hour dark cycle with standard food and water provided ad libitum. Experimental glaucoma was induced by translimbal laser photocoagulation of the trabecular meshwork. The treatment details have been described previously.[31] Laser treatment was administered in the left eye of each rat. The contralateral eye was untreated. Intraocular pressure (IOP) in both eyes was measured just before treatment and regularly after treatment. Details of IOP measurements and IOP time courses of each animal are given in the Supplementary Materials.

After treated eyes were exposed to elevated IOP for approximately 2 weeks, treated eyes of each animal were removed and prepared for optical imaging and immunohistochemical study. To serve as controls, some of the contralateral untreated eyes were also removed and studied. Tissue preparation followed previously developed procedures.[35] An eye cup of 5-mm diameter was excised and placed in a dish of warm (33°–35° C) oxygenated physiologic solution. After removal of the vitreous, the retina was dissected free of the RPE and choroid and then draped across a slit in a membrane with the photoreceptor side against the membrane. A second, thinner membrane with a matching slit was put on the RNFL surface to gently flatten the retina. The preparation was carried out with intense white illumination, which thoroughly bleached the visual pigment in the photoreceptors and ensured that the reflectance in this layer remained constant.

The mounted retina was then placed in a chamber perfused with a warm physiologic solution to maintain the tissue in a living state.

All experiments adhered to the ARVO Statement for the Use of Animals in Ophthalmic and Vision Research. The protocol for the use of animals was approved by the Animal Care and Use Committee of the University of Miami.

### Measurement and Calculation of RNFL Reflectance

Retinal nerve fiber layer reflectance was measured by a multispectral imaging microreflectometer. The device and measurement of retinal reflectance have been described in detail previously and are briefly described in the Supplementary Materials and Supplementary Figure S1.[24,35] The output of the microreflectometer is a relative reflectance calculated by calibration with a diffuse white reflector, expressed in units of percent incident light reflected.

Retinal nerve fiber bundles appear as bright stripes in reflectance images (Fig. 1). Retinal nerve fiber layer reflectance was measured for bundle areas located at distances from the ONH center of 300, 400, 500, 600, and 700 μm. Reflectance measured on bundle areas includes light reflected from the RNFL and its underlying tissue. Because the weak scattering of the RNFL causes little attenuation to an incident beam, we assumed that the reflectance from deep layers was approximately the same as that from nearby gap areas between bundles. Areas were chosen both on bundles and on nearby gaps between bundles (Fig. 1), and the average reflectance of gap areas ($R_{gap}$) was then subtracted from the total reflectance ($R_{total}$) measured on the bundle areas to get an estimate of the bundle reflectance alone, that is, $R = R_{total} - R_{gap}$. Hereafter, the relative reflectance $R$ denotes the reflectance of the RNFL alone and is simply called reflectance.

The value of $R$ depends on measurement geometry. For each bundle, the incident and scattering angles were calculated from the relative positions of the bundle, light source, and camera. As in previous work,[7,13] the incident angle of a bundle was defined as the angle between the incident ray and a plane perpendicular to the bundle; the scattering angle was defined as the angle between incident and scattering planes, where the incident plane contained the incident ray and the bundle and the scattering plane contained the reflected ray and the bundle. The three-dimensional (3D) orientation of a bundle was calculated from its projected angles in images that were taken at two additional camera positions.

### Measurement and Calculation of RNFL Retardance and Birefringence

After reflectance measurements, the same retinas were transferred to an imaging micropolarimeter and RNFL retardance ($\delta$) was measured in transmission. The device and measurement procedures have been described in detail previously and are given in the Supplementary Materials.[16,20] Birefringent nerve fiber bundles were observable with the micropolarimeter under conditions in which the polarization state exiting the tissue was nearly extinguished by the polarization detector (C'A, see Supplementary Fig. S2A). Because the polarization detector provided only a limited number of states, some bundles could not be seen by the micropolarimater.[20] Retardance was measured along a bundle at distances from the ONH center of 300, 400, 500, 600, and 700 μm to form a retardance profile. The measurement accuracy of $\delta$ was 0.05 nm.

Because RNFL birefringence shows little variation with wavelength,[16] in this study $\delta$ was measured at 500 nm only. To calculate birefringence ($\Delta n$), the thickness ($T$) of bundle areas
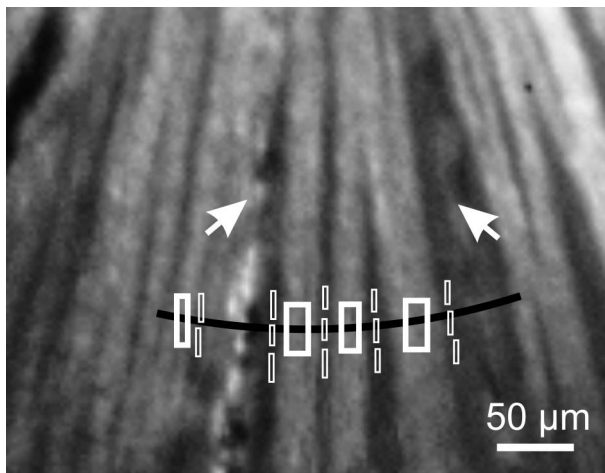
**FIGURE 1.** Reflectance image of normal bundles at 440 nm. Nerve fiber bundles appear as *bright stripes* and are separated by gaps, seen as *darker spaces* between bundles. *Black arc* with a radius of 400 μm indicates a fan-shape sector centered at the ONH center. *Thick boxes*: bundle areas crossed by the arc; *thin boxes*: gap areas; *arrows*: blood vessels.

was measured from confocal images of the RNFL (details are in the next section). $\Delta n$ was then calculated as the ratio of δ and $T$. $\Delta n$ is a dimensionless quantity expressed in units of nm/μm.

In both reflectance and retardance measurements, a series of images were taken. To compensate for possible tissue shift during measurements, each set of images was registered by horizontal and vertical translation.

## Confocal Imaging of RNFL and Measurement of Its Thickness

After optical measurements, which were completed in approximately 40 minutes for both reflectance and retardance measurements, the mounted retina was fixed in 4% paraformaldehyde for 30 minutes at room temperature and rinsed thoroughly in PBS. The tissue then was removed from the membranes for further immunohistochemical staining and confocal imaging. The detailed staining procedures have been

published previously and are given in the Supplementary Materials.[34]

The fluorescently stained retina was imaged by a confocal laser scanning microscope (Leica TCS SP5; Leica Microsystems, Wetzlar, Hesse, Germany). A 40× oil objective provided en face images of a retina with a field of view of 389 × 389 μm and a resolution limited to the sampling density of 0.76 μm per pixel. To cover all bundles emerging from the ONH, at least a 3 × 3 tiled array of images was taken that covered a retinal area of 1.2 × 1.2 mm with the ONH at the center (Fig. 2B). For each array position, en face images were collected at evenly spaced positions in depth (1 μm apart in tissue) starting from the RNFL surface through the retina to a depth at least including the ganglion cell layer. The retina was then reconstructed in 3D and cross-sectional (CS) images were synthesized from the reconstruction with customized software (Figs. 2C–E).

To identify the location of an individual nerve fiber bundle measured optically, the en face confocal image of a retina was registered onto the optical images of the same retina by matching the blood vessel patterns (Figs. 2A, 2B). Bundle areas defined in optical images were then transferred into the confocal images. Cross-sectional images along lines crossing the bundle areas were obtained from a reconstructed 3D confocal image. The RNFL was identified as an intensely stained structure in the top layer of the retina (Figs. 2C–E). To measure RNFL thickness, a merged CS image of stained F-actin, MTs, and neurofilaments (NFs) was used. The thickness of an individual bundle was measured as the average thickness within a window centered on the bundle and half as wide (dashed lines in Figs. 2C–E). In this study, the axial resolution of the confocal microscope calculated for the longest excitation wavelength was 0.7 μm and the step size of the depth scan was 1 μm. Measurement uncertainty of the RNFL thickness did not exceed 2 μm, which was used as the measurement accuracy for RNFL thickness.

### Data Analysis

Three kinds of data were available from each retina analyzed: (1) reflectance spectra at several positions along all bundles that matched the criteria set for scattering and incident angles (criteria established using data acquired in normal bundles; see Results), (2) retardance profiles for all bundles that were visible in polarization images,[20] and (3) a severity grade for F-actin
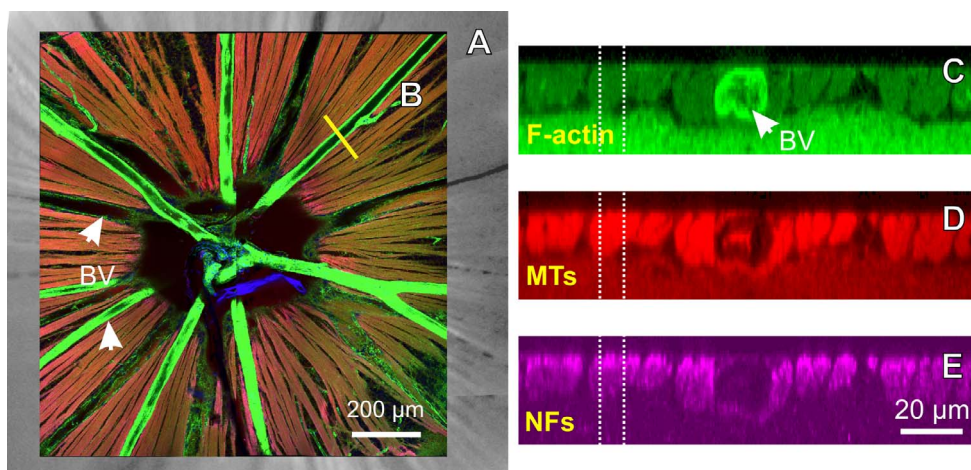


**FIGURE 2.** Confocal images of a whole-mounted normal retina. (**A**) Retinal image in reflectance. (**B**) Merged en face image of the same retina with F-actin, MT, and NF stain. Staining variation across the image was due to tissue curvature resulting in bundles imaged at different depths. (**C–E**) Cross-sectional images of F-actin, MT, and NF stain along the *yellow line* in (**B**). *Dashed lines*: the window used for calculating bundle thickness. BV, blood vessel.
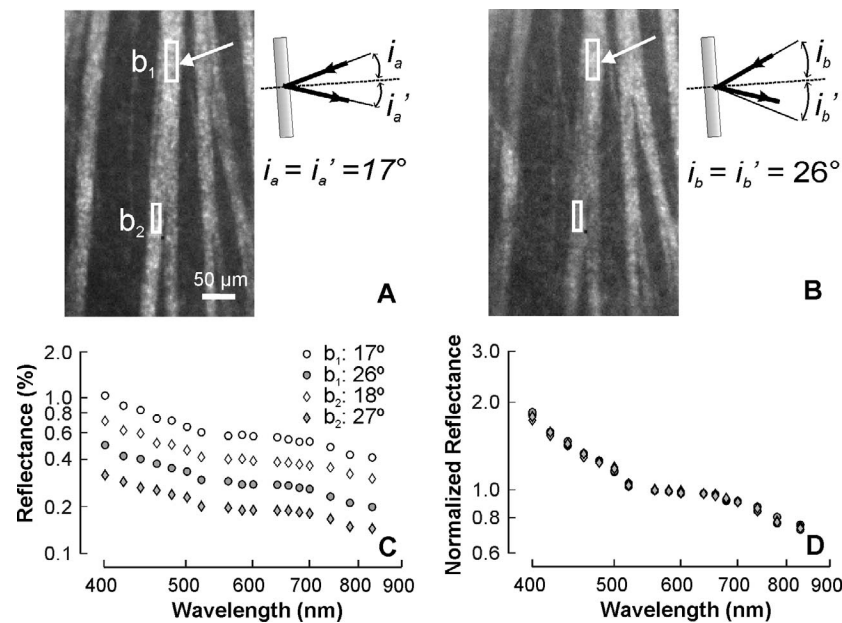
**FIGURE 3.** Retinal nerve fiber layer reflectance spectra measured at on-peak and off-peak reflectance. Images taken at 500 nm with the scattering angle at 178°. (**A**) Bundle areas (b1 and b2) imaged at maximum (on-peak) reflectance with incident angles ($i_a$ in *inset*) of 17° and 18° for b1 and b2, respectively. *Inset*: a side view of the measurement geometry for b1. The *dashed line* is perpendicular to the bundle, which is tilted 4°. The *thin lines* illustrate the reflection geometry of light scattering by a cylinder at direct backscattering. The *thick lines* with *arrows* indicate the incident beam provided by the light source and the reflected beam detected by the camera; that is, the image in (**A**) was taken with the configuration of the bundle (b1) orientation, and the positions of the light source and camera that meets the geometry of light scattering by cylinder. (**B**) Bundle areas imaged at off-peak reflectance with the camera position unchanged and the incident angle ($i_b$) changed to 26° and 27° for b1 and b2, respectively. The bundle appeared dimmer. *Inset*: similar to the *inset* in (**A**), the *thin lines* illustrate the incident beam and predicted reflected beam. Because in this setting the camera position did not change, the camera detected a reflected beam (the *lower thick line* with *arrow*) that was off the predicted beam; that is, the bundle was measured at off-peak reflectance. (**C**) Reflectance spectra measured at on-peak and off-peak reflectance for the bundle areas of $b_1$ and $b_2$. At off-peak reflectance, the mean reflectance of the spectra decreased by 50% for $b_1$ and 52% for $b_1$ and $b_2$. (**D**) The normalized spectra were nearly identical for the on-peak and off-peak measurements. All spectra reported in this study are plotted on log-log coordinates.

distortion in fan-shaped areas around the ONH, with each area having relatively similar appearance of F-actin in confocal images. To reduce bias, the F-actin appearance was graded without knowledge of the optical properties. Registration of the reflectance and retardance images identified those bundles that had measurements of both optical properties. Finally, registration of the optical and confocal images provided a severity grade for the sector in which bundles had optical measurements. The sector width was determined by the extent of bundles that had both reflectance and retardance measurements. Most of the sectors had angular widths of approximately 30° and sectors in the same retina were well separated (see Fig. 9 for details). Additionally, the thickness of each bundle was measured in the confocal images.

All sectors in all retinas for which the three measurements were available were analyzed. For each sector, bundle areas were defined at different distances from the ONH center ($r = 300$–$700$ μm). At each $r$, all bundles with approximately uniform background in optical images and containing no blood vessels were analyzed (Fig. 1). The averages of the reflectance spectrum, birefringence, and thickness of these bundle areas were then used to represent the properties of the RNFL at the location. Note that within a sector, different numbers of bundles were averaged at different radii due to the change of arc size. For each sector, at least two bundles at $r = 300$ μm and four to eight bundles at each $r \geq 400$ μm were analyzed and then averaged (the number of bundles averaged for each $r$ in each sector is given in Supplementary Table S1). Unless otherwise stated, the average reflectance spectrum, birefringence profile, and thickness were used in comparisons among sectors.

Data analysis and confocal image reconstruction were implemented with customized software programmed in Matlab (Matlab Version 2012b, The MathWorks, Inc., Natick, MA, USA).

## RESULTS

Fifteen rats were used in the study, with 11 rats treated to develop ocular hypertension and 4 rats without any treatments. All 11 treated retinas were used in the study. Eight retinas were used as control with four retinas from each of the four normal rats and four retinas from contralateral eyes of treated rats. Because no differences were found for the optical properties and cytostructure of the retinas from the normal rats and the contralateral untreated eyes, these eight retinas served as normal controls.

### Reflectance Spectrum and Birefringence of Normal Bundles

Due to the property of directional reflectance of the RNFL, bundle reflectance ($R$) depends on the measurement geometry. Figure 3A shows a bundle area (b1) that was measured at maximum (on-peak) reflectance with the light source and camera positions set to satisfy the geometry for light scattering by cylinders (details in the legend for Fig. 3A inset). Figure 3B shows an example of the same bundle measured at off-peak reflectance. With a 4° change of the incident angle and without change of the camera position, the same bundle area appeared dimmer (Fig. 3B). At every wavelength, the measured $R$
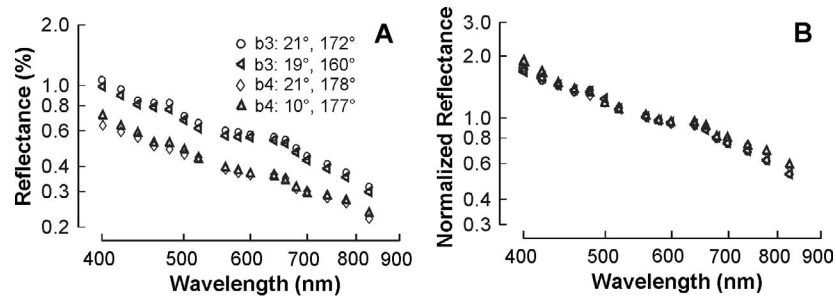
**FIGURE 4.** Dependence of RNFL reflectance spectrum on incident and scattering angles. (**A**) On-peak spectra of two bundles from two normal retinas. Bundle b3 was measured with similar incident angles, but the scattering angle changed from 172° to 160°. Bundle b4 was measured with similar scattering angles, but the incident angle changed from 21° to 10°. (**B**) Normalized spectra showing that the spectral shape is similar with changes of either the incident angle or scattering angle.

decreased to approximately 50% of its on-peak reflectance (Fig. 3C).

To compare the similarity of the measured RNFL reflectance spectra, each reflectance spectrum was normalized to the average reflectance at 560 to 600 nm. The shapes of the RNFL reflectance spectra in Figure 3C were nearly identical (Fig. 3D).

Because the shape of the RNFL reflectance spectrum can vary with the incident and scattering angles,[7] we examined this variation over a limited range, as illustrated in Figure 4. Figure 4A shows the spectra of two bundles from different retinas that were measured at different incident and scattering angles. Both bundles were measured at on-peak reflectance. The two spectra for bundle b3 were obtained with similar incident angles (19° and 21°, respectively). Changing the scattering angle from 172° to 160° caused *R* to decline slightly at all wavelengths, with the decrease ranging from 3.1% to 6.7%. Overall, the spectral shape remained nearly identical. The two spectra for bundle b4 were obtained with similar scattering angles (178° and 177°, respectively). Changing the incident angle from 21° to 10° caused *R* to increase, with a greater increase at short wavelengths (e.g., 10.4% at 400 nm), again the overall spectral shapes were similar. The normalized

spectra in Figure 4B show that a 12° change of incident angle or a 11° change of scattering angle result in very little change in their overall shape. We conclude that the shape of the RNFL reflectance spectrum is not very sensitive to the measurement geometry as long as the ranges of incident and scattering angles are restricted. In this study, the incident and scattering angles ranged from 7° to 25° and 163° to 179°, respectively. The bundles, however, were not all measured at on-peak reflectance.

Thirty-two sectors in eight control retinas (four sectors in each retina) were analyzed. Consistent with our previous report, bundles in all 32 sectors showed intense and uniform stain of F-actin, MTs, and NFs.[34] No apparent structural abnormality was noticed across the retina. Reflectance spectra were measured at several distances from the ONH within each sector. Occasionally a single bundle could be measured at all distances. Figures 5A through 5C show the results for one such bundle. Figure 5A shows the bundle and gap areas used to measure the reflectance at a radius (*r*) of 500 μm. The centers of the measurement areas for other radii along the same bundle are indicated by dots. *R* decreased with increase of wavelength (Fig. 5B). At any given wavelength, *R* decreased with distance
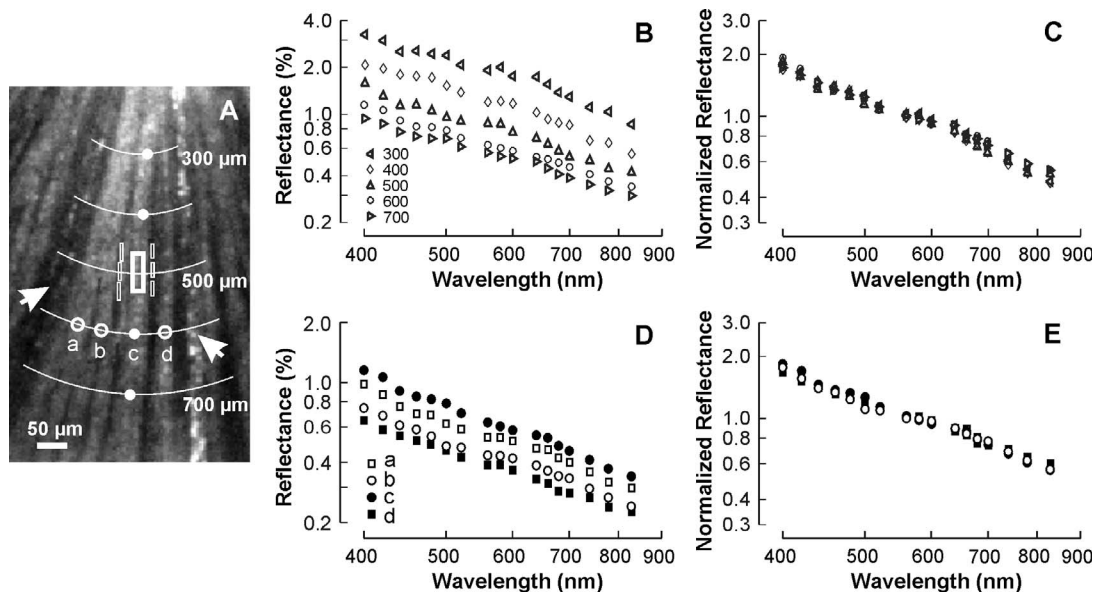


**FIGURE 5.** Reflectance spectra in a normal sector. (**A**) Reflectance image of normal bundles at a wavelength of 500 nm. The arcs indicate distances from the ONH center of *r* = 300 to 700 μm. *Arrows*: blood vessels. (**B**) Reflectance spectra along one bundle with areas indicated in (**A**) as *white dots* and *thick box*. (**C**) Normalized reflectance spectra of (**B**). (**D**) Reflectance spectra of neighboring bundles. Bundle areas indicated in (**A**) as *white circles* and a *dot* and marked as a–d at *r* = 600 μm. (**E**) Normalized reflectance spectra of (**D**). The normalized spectra in (**C**) and (**E**) showing similar spectral shape along a bundle and within a sector. Incident angles: 16° to 20°, scattering angles: 174° to 177°.
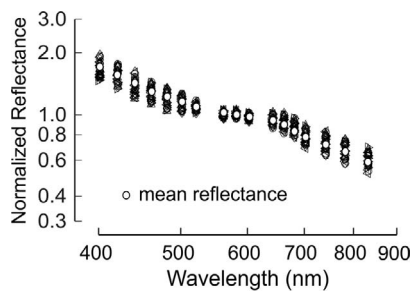
**FIGURE 6.** Reflectance spectra of normal nerve fiber bundles. Thirty-two sectors from eight normal retinas. Each spectrum was the average of three to six bundles measured at $r = 500$ μm and normalized to the mean reflectance at 560 to 600 nm. Incident and scattering angles ranging from 7° to 25° and 162° to 180°, respectively.



**FIGURE 7.** Birefringence ($\Delta n$) profiles along normal nerve fiber bundles. (**A**, **B**) Bundle thickness and retardance decrease with the increase of distance from the ONH along the bundle in Figure 5. (**C**) $\Delta n$ is approximately constant along the bundle. (**D**) Profiles of the mean $\Delta n \pm 2$ SD of 32 sectors from eight normal retinas. *Gray bar* shows the overall range of normal $\Delta n$. The *error bar* at the right side of (**D**) shows the maximum variation ($\pm 2$ SD) in $\Delta n$ across radii for individual sectors.

from the ONH center due to thinning of the bundle peripherally. The normalized reflectance spectra (Fig. 5C) show that the shape of the reflectance spectrum was similar along the bundle. Figure 5D shows the reflectance spectra of neighboring bundles at $r = 600$ μm. The normalized spectra (Fig. 5E) indicate that the shape of the reflectance spectrum was also similar among bundles at the same $r$.

The spectra in Figure 4 from two bundles in two different retinas suggest that the shape of the reflectance spectrum is similar among normal bundles. Figure 6 shows normalized reflectance spectra of 32 normal sectors measured at $r = 500$ μm. The similarity of these spectra suggests that the shape of the RNFL reflectance spectrum is a robust feature that can be used to study changes of RNFL reflectance in diseased retinas.

Birefringence was measured for the same bundles as reflectance measurements. Figures 7A and 7B show an example of the thickness and retardance profiles along the bundle displayed in Figure 5. Both $T$ and $\delta$ declined with the increase of distance from the ONH center. The corresponding $\Delta n$, however, varied little between $r = 300$ μm and 700 μm (Fig. 7C). Figure 7D summarizes $\Delta n$ profiles of 32 sectors, with each $\Delta n$ profile the average of bundles within the same sector. For each sector, $\Delta n$ did not change very much with radius, with a maximum SD of 0.02 nm/μm. The average values along bundles, however, were significantly different among sectors ($P < 0.0001$), with $\Delta n$ ranging from 0.24 to 0.39 nm/μm. Unpublished data show no consistent pattern of $\Delta n$ profiles around the ONH in normal retinas; sector location, therefore, was not considered when comparing $\Delta n$ of treated bundles with normal values. $\Delta n$ was not correlated with $T$.

## Distortion of Axonal Cytoskeleton in Hypertensive Retinas

Eleven treated retinas were analyzed in this study. The baseline IOP of treated eyes before treatment (10.2 ± 0.6 mm Hg) was not statistically different from the control retinas (10.2 ± 0.5 mm Hg; $P = 0.6$, $t$-test). The mean IOP in 2 weeks ranged from 16.7 to 23.8 mm Hg, with the mean peak IOP of 41.0 ± 8.5 mm Hg (individual IOP time courses are in Supplementary Fig. S3). The rat model of glaucoma used in this study induced characteristic changes of axonal cytoskeletal components, which we have reported previously.[31,34] These changes, confirmed in this study, include the findings that various degrees of cytoskeletal distortion occur within a single treated retina, that the distortion starts early near the ONH, and that distortion of F-actin occurs before change of MTs and NFs.[34]

The goal of this study was to demonstrate how the optical properties of the RNFL, specifically the RNFL reflectance spectra and $\Delta n$ profiles, change in bundles with different
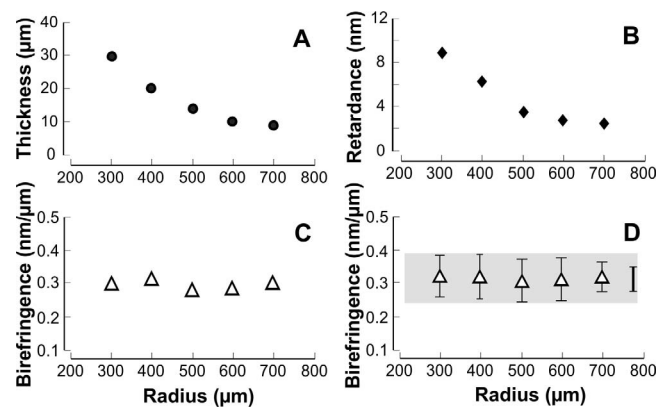
degrees of ultrastructural damage. Because F-actin distortion precedes change of MTs and NFs, the appearance of F-actin stain was used to grade the degree of damage.[34]

A grading system was developed to describe F-actin distortion and identify retinal sectors with different degrees of damage. This distortion and the grading system are illustrated in Figure 8, which shows an example of changes of F-actin around the ONH and along bundles. Bundles in retinal sectors A1 and A2 are normal-looking in the en face image. Their corresponding CS images at $r = 500$ μm show uniformly stained F-actin within bundles (Fig. 8B), similar to the normal (Fig. 2B). The CS image of A1 near the ONH ($r = 300$ μm) is also nearly normal-looking; however, the CS image of A2 at $r = 300$ μm is less uniform compared with that at $r = 500$ μm. Nonuniform stain suggests distortion of cytoskeletal structure. For bundles in sector A3, distortion of F-actin in the en face image and nonuniform stain in the CS image both become apparent. Sector A4 shows an example of a retinal sector in which severe damage of axonal cytoskeleton and obvious thinning of RNFL occur. Although Figure 8A shows only a single en face image, multiple en face images at different depths in the RNFL were examined before assigning a grade to a retinal sector.

From here on, we denote the F-actin appearance of a sector with one of the grades A1 through A4 based on its similarity to a sector in Figure 8. For each retina, a grade was assigned to each clock-hour sector around the ONH. For the 11 treated retinas, the distribution of grades A1 though A4 did not show location dependence ($P = 0.998$, tested by Friedman's nonparametric 2-way repeated measures test). Note that not all sectors across the retina were studied optically. The retinal sectors available for this study were limited by the requirements that the sectors must have all of the measurements of reflectance, birefringence, and cytostructure, and RNFL reflectance was measured near direct backscattering (scattering angle ranged from 162°–180°). Figure 9 depicts the studied retinal sectors for each retina.

Twenty-five sectors in 11 treated retinas were studied. For each studied sector, average thickness measured at $r = 300$ μm was compared with a normal value (mean ± SD of 20.2 ± 8.4 μm) derived from 146 normal bundles with randomly distributed bundle orientation (92 normal bundles in this study and an additional 54 normal bundles measured in other
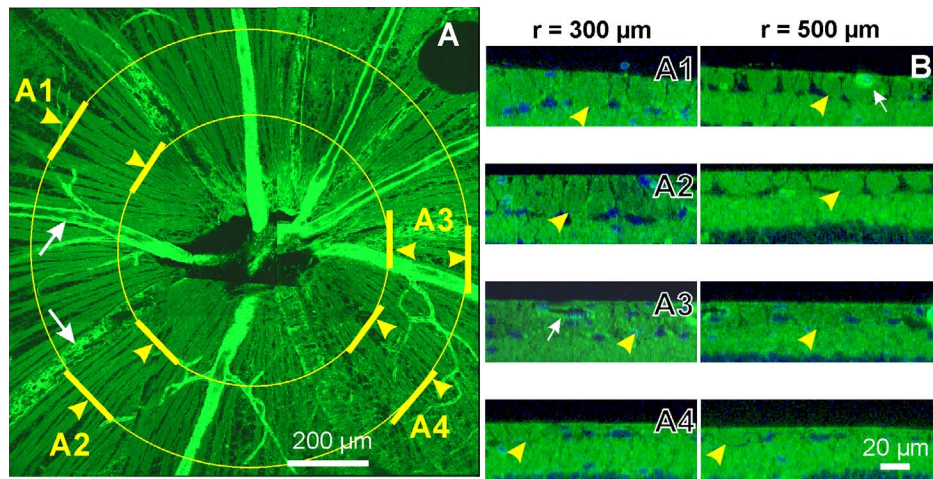
**FIGURE 8.** Confocal laser scanning microscopy images of nonuniform cytoskeletal damage in a hypertensive retina stained with F-actin. (**A**) En face image of a $3 \times 3$ tiled array centered on the ONH. *Circle radii*: 300 and 500 μm. (**B**) Cross-sectional images with F-actin stain along the lines defined in (**A**). *Yellow arrows*: bundles analyzed for reflectance and birefringence; *white arrows*: blood vessels. The appearance of nerve fiber bundles varies across retinal sectors from normal-looking in (**A1**), to subtle distortion near the ONH in (**A2**), moderate distortion in (**A3**), and severe distortion and obvious thinning in (**A4**). Note that tissue curvature meant that bundles across the retina were not all imaged at the same depth in (**A**) and that distortion was evaluated from multiple en face images at different depths of the RNFL.

studies). All four sectors graded A1 and five sectors graded A2 had thickness not significantly different from normal ($P > 0.37$). Six of 10 sectors graded A3 also had normal thickness, whereas the other 4 sectors were thinner than normal ($P < 0.043$, 1-way ANOVA followed by post hoc least significant difference test). All six sectors graded A4 were significantly thinner than the normal ($P < 0.001$), with average $T$ ranging from 5.4–9.6 μm. A summary of RNFL thickness and birefringence measured in all studied sectors is given in Table S1 in the Supplementary Materials.

Below we present the reflectance spectrum and birefringence of treated NF bundles in three groups. The first group, mild cytoskeletal distortion, includes bundles that fall in sectors graded A1 with nearly normal-looking bundles, and those graded A2 that show no apparent cytoskeletal change away from the ONH but do show change near the ONH. The second group, moderate cytoskeletal distortion, corresponds to sectors graded A3, and the third group, severe cytoskeletal distortion, corresponds to sectors graded A4.

## Optical Measurements: Mild Cytoskeletal Distortion

Bundles in sectors graded A1 and A2 showed two patterns of behavior, which are illustrated in Figure 10 for two bundles in Figure 8. Figures 10A and 10C, respectively, show the normalized reflectance spectra of the indicated bundles in sectors A1 and A2 of Figure 8. For display clarity, the figures show only the spectra measured at $r = 300$, 500, and 700 μm. The normalized reflectance spectra were similar to the normal at wavelengths greater than 460 nm but showed a decrease at short wavelengths ($\leq 440$ nm) as the bundle neared the ONH.

Figure 10B shows the $\Delta n$ profile of the bundle in sector A1. For this bundle, the $\Delta n$ was approximately constant along the bundle and within the normal range. In contrast, Figure 10D shows that the $\Delta n$ profile of the bundle in the A2 sector decreased significantly at $r = 300$ μm compared with its values at $r = 400$ to 700 μm, although the mean $\Delta n$ of the profile was within the normal range.

For nine retinal sectors graded A1 or A2 from five retinas, the reflectance spectra of all analyzed sectors showed change at short wavelengths as bundle areas neared the ONH. In contrast, five of these sectors (four A1 and one A2 in Fig. 11A) had the $\Delta n$ profiles similar to Figure 10B, whereas the other four sectors (all A2 in Fig. 11B) showed $\Delta n$ that decreased at $r = 300$ μm compared with its value measured at $r \geq 400$ μm, similar to Figure 10D.

## Optical Measurements: Moderate Distortion of Cytoskeleton

Compared with bundles with mild cytoskeletal distortions, the normalized reflectance at short wavelengths for bundles with moderate cytoskeletal distortion (grade A3) demonstrated a greater decrease at $r = 300$ μm and the decrease also occurred at other distances. Figure 12A shows the reflectance spectra of the indicated single bundle in retinal sector graded A3 of Figure 8. The normalized reflectance at short wavelengths decreased
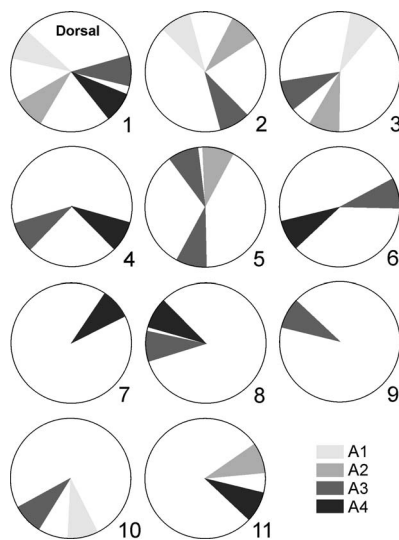


**FIGURE 9.** Schematic diagram of the 25 studied retinal sectors in 11 treated retinas. The *gray shades* indicate the structural severity grade assigned to each sector (**A1–A4**). Retinal orientation moving clockwise: dorsal, rostral, ventral, and caudal.
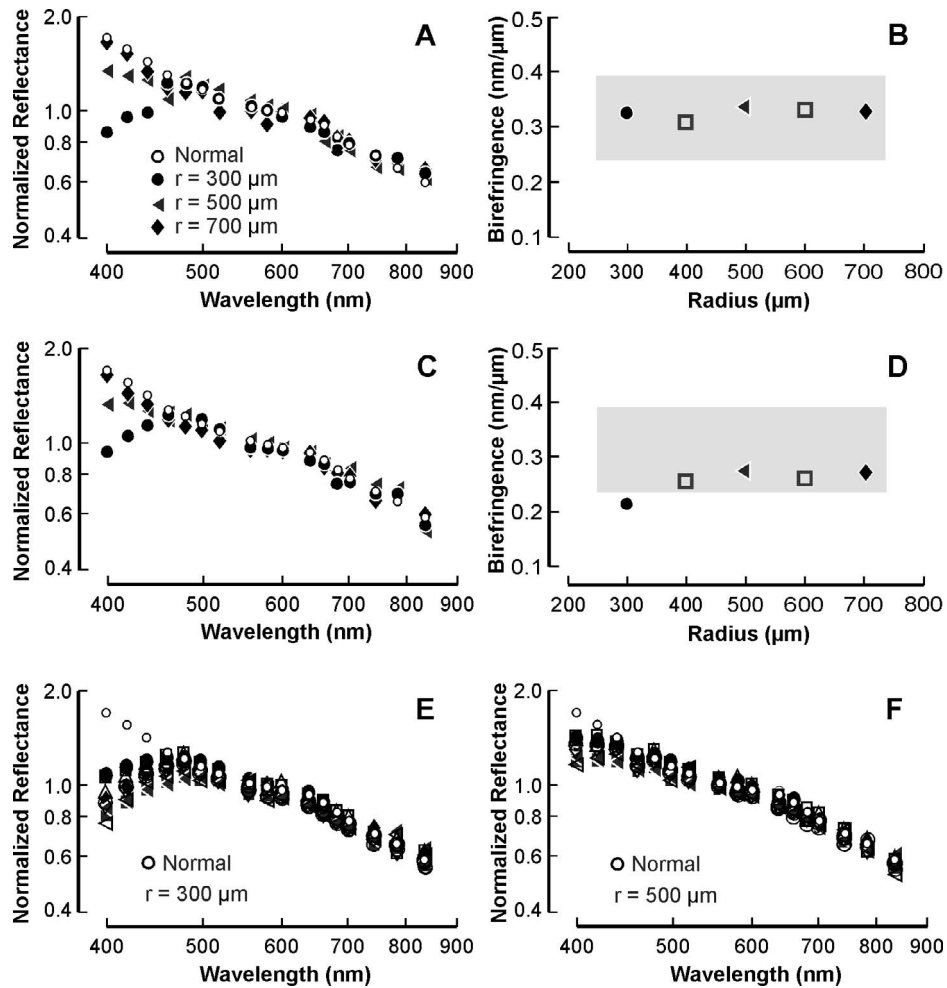
**FIGURE 10.** Reflectance spectra and birefringence (*Δn*) profiles of bundles with no obvious cytoskeletal change in the peripheral retina. (**A**) and (**B**) for the indicated single bundle in (**A1**) of Figure 8; (**C**) and (**D**) for the indicated single bundle in (**A2**) of Figure 8. The normalized reflectance spectra (**A**, **C**) were similar to the normal at wavelengths ≥460 nm; however, the reflectance at short wavelengths decreased as bundle areas neared the ONH. The *Δn* profiles were either similar to the normal (**B**) or showed decreased *Δn* at *r* = 300 μm (**D**); *gray bar*: normal range of *Δn*. (**E**, **F**) show the normalized reflectance spectra of all sectors graded as A1 and A2. Spectra measured at *r* = 700 μm, which were similar to the normal, do not show.

more than in sectors A1 and A2 as the bundle areas neared the ONH. The corresponding *Δn* profile (Fig. 12B) shows that *Δn* at all *r* fell below the normal range.

Figure 13 shows another example of a grade A3 retinal sector in a different retina. Stain of F-actin and MTs in CS images were less uniform compared with the normal and

showed more prominent structural distortion than sector A3 of Figure 8. The normalized reflectance of the indicated bundle (Fig. 13E) shows that the decrease of the reflectance at short wavelengths occurred at all *r*. The spectra also show that the normalized reflectance at long wavelengths became higher than the normal (*P* = 0.025), especially at *r* = 300 μm (*P* <
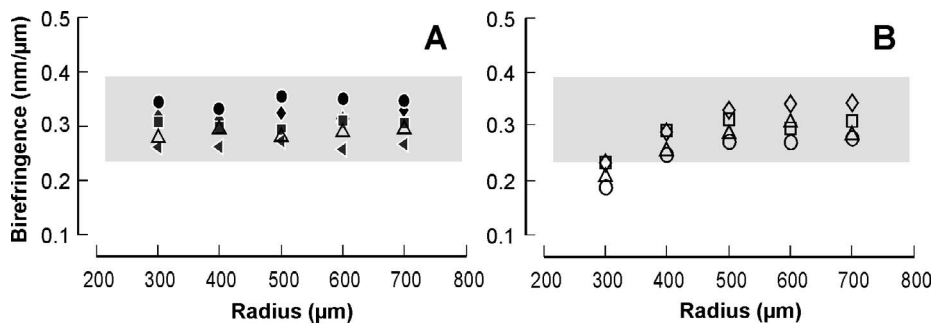


**FIGURE 11.** Birefringence (*Δn*) profiles for retinal sectors with no obvious cytoskeletal change in the peripheral retinal region (grades A1 and A2). *Δn* along bundles were either approximately constant and within the normal range (**A**) or showed a decrease of *Δn* near the ONH (**B**). Each data point was the average of two to eight bundles. *Solid symbols*: grade A1; *open symbols*: grade A2. *Gray bar*: normal range of *Δn*.
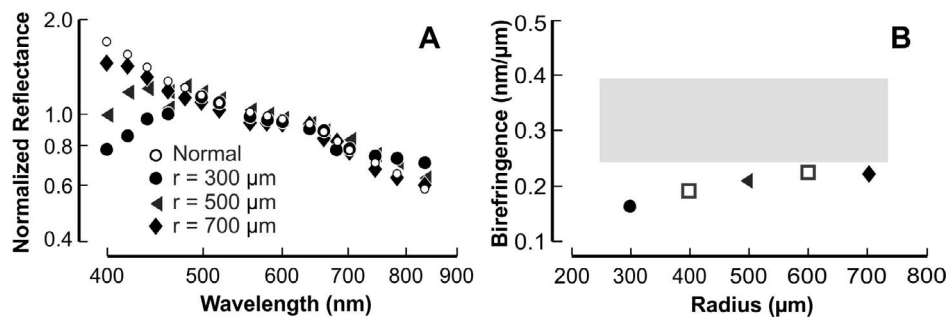
**FIGURE 12.** Reflectance spectra and birefringence (Δn) profile of a single bundle with moderate cytoskeletal distortion in Figure 8 (sector A3). (**A**) The normalized reflectance spectra at short wavelengths decreased as the bundle area neared the ONH. (**B**) Δn profile is below the normal range (*gray bar*).

0.001). The corresponding Δn profile of the bundle fell below the normal range.

For 10 retinal sectors graded A3 in nine retinas, all showed change of the reflectance spectra near the ONH, both at short wavelengths and at long wavelengths (Fig. 14A). Their Δn profiles were all below the normal range (Fig. 14B).

### Optical Measurements: Severe Distortion of Cytoskeleton and Thinning of RNFL

For bundles in retinal sectors with severe cytoskeletal change in en face images and thinning in CS images (grade A4), the reflectance spectra were nearly flat across wavelengths. Figure 15A shows the reflectance spectra of the indicated single bundle in sector A4 of Figure 8. The bundle thickness at r = 300 μm was 9.5 μm, significantly lower than the normal. Surprisingly, the corresponding Δn profile (Fig. 15B) was within the normal range. The Δn of bundles with severe damage, however, also could have a Δn profile falling below the normal range. Figures 15C and 15D show the reflectance spectra and Δn profiles of six severely damaged retinal sectors, each from a different retina (sectors A4 in Fig. 9). The average thickness at r = 300 μm was less than 9.6 μm for all sectors.

Although for thin bundles with high Δn the inaccuracy of Δn could be substantial (Supplementary Table S1), no amount of the error can remove the fact that bundles with significant birefringence were observed for the retinal sectors of grade A4.

### DISCUSSION

This study used a rat model of glaucoma and isolated retinas to provide insight into how the RNFL reflectance spectrum and birefringence change in retinal nerve fiber bundles with different degrees of cytostructural damage. Use of isolated retinas eliminated the confounding effects of other ocular tissues, including the cornea and lens, on measurements of the RNFL optical properties.

In normal rat retinas, we found that the shape of the RNFL reflectance spectrum, as expressed by the normalized reflectance spectrum ($R_N$), did not change along bundles, and RNFL birefringence (Δn) was approximately constant along bundles. These results suggest that the structures that contribute to RNFL reflectance and birefringence do not change very much along bundles in normal tissue. The underlying anatomic bases for RNFL reflectance and birefringence are not identical, however, as studies show that in rodent retinas, MTs are the
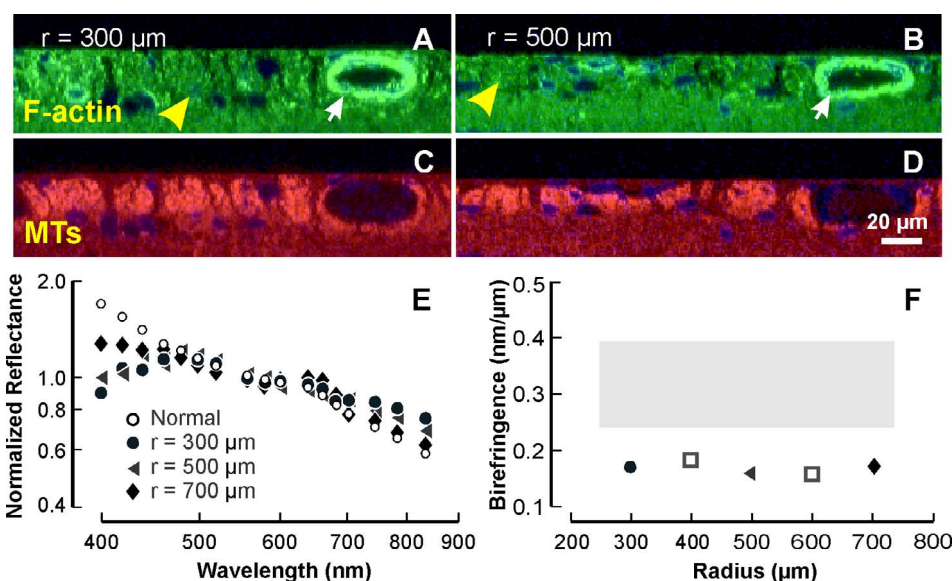


**FIGURE 13.** Reflectance spectra and birefringence (Δn) profile of another bundle in a different retina with moderate cytoskeletal distortion (grade A3). (**A–D**) Cross-sectional images showing distortion of F-actin and MTs with bundles. Images merged with 4′,6-diamidino-2-phenylindole stain of nuclei (*blue*). *White arrow*: blood vessel. (**E**) Reflectance spectra of the indicated bundle in (**A**) and (**B**) (*yellow arrow*). (**F**) Δn at all r was below the normal (*gray bar*).
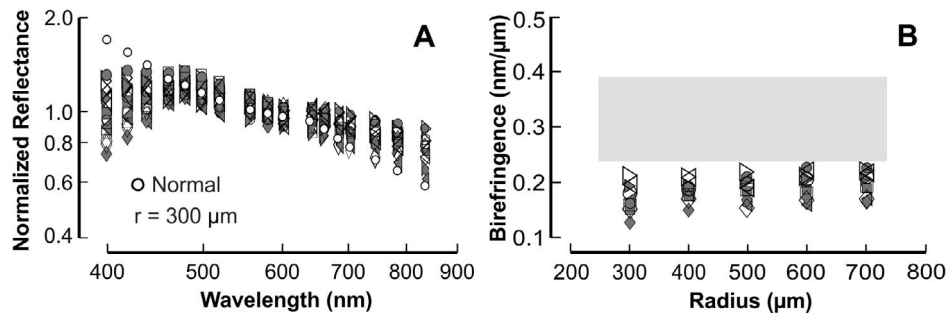
**FIGURE 14.** Reflectance spectra and birefringence (*Δn*) profiles of bundles with moderate cytoskeletal distortion (grade A3). Ten sectors from nine treated retinas. (**A**) Compared with the normal, the normalized reflectance spectra at $r = 300$ μm showed a decrease at short wavelengths and an increase at long wavelengths. (**B**) *Δn* at all *r* was below the normal range (*gray bar*).

dominant structures for RNFL birefringence, whereas MTs contribute less than 50% to RNFL reflectance. It is known that glaucoma damages the ultrastructure of ganglion cell axons and different structures (e.g., MTs, NFs, F-actin) respond differently to the damage.[26,29,33,34,36] Hence, under the circumstance of glaucomatous damage to the RNFL, the optical properties of RNFL reflectance and birefringence are expected to change, but these changes may not be similar.

The damage to the axonal cytoskeleton induced by the rat model of glaucoma used in this study varies from undetectable to severe and, in addition, different degrees of structural damage can occur within a single retina, as reported previously.[31,34] This feature of the model allowed us to compare the change of RNFL optical properties with the degree of damage severity, as assessed by the severity of F-actin distortion. To prevent bias, we graded the severity of F-actin distortion within retinal areas without knowledge of their optical properties, and have included data from all nerve fiber bundles for which optical measurements were possible. It must be noted that, although the association between F-actin distortion and damage severity is plausible, the use of F-actin

distortion as a measure of overall structural damage has not been independently validated, a limitation of the study.

If one accepts our grading system as a measure of damage, the principal finding of the study is that, with the exception of birefringence in some severely damaged sectors (discussed later), as damage severity increases, both $R_N$ and *Δn* depart further and further from normal. Thus, optical properties can serve as an accessible surrogate for cytoskeletal damage. In addition, detectable change in both optical properties occurs before change in RNFL thickness and, in some cases, even before apparent cytoskeletal change. Thus, these properties also may serve as sensitive indicators of early disease.

The pattern of change of optical properties with severity observed in this study suggests that axonal damage starts at the ONH and then propagates peripherally along bundles, following the pattern for cytoskeletal damage found previously and confirmed here (Fig. 8B).[9,34] The earliest change seen, a short-wavelength decrease in $R_N$ that is apparent even in sectors with normal-looking F-actin (grade A1), is larger in spectra acquired closer to the ONH (Figs. 10A, 10C). With moderate damage (grade A3), $R_N$ begins to flatten, with a greater decrease at short wavelengths and an increase at long
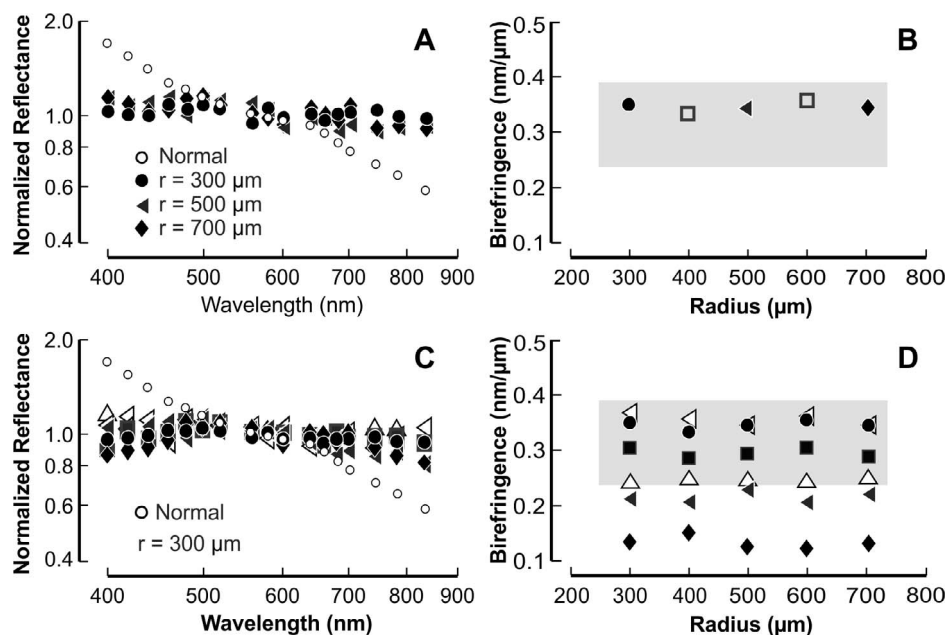


**FIGURE 15.** Reflectance spectra and birefringence (*Δn*) profiles of sectors with severe distortion of cytoskeleton and thinning of RNFL (grade A4). (**A, B**) Reflectance spectra and *Δn* along the indicated single bundle in sector (A4) of Figure 8. (**C, D**) Reflectance spectra and *Δn* profiles of six sectors, each from a different retina. Reflectance spectra at $r = 300$ μm are shown. All reflectance spectra appear flat. *Δn* is either within or below the normal range (*gray bar*).

wavelengths. Although change also occurs more peripherally, it is still larger near the ONH (Figs. 12A, 13A). Finally, with severe damage and thinning (grade A4), $R_N$ becomes flat at all distances from the ONH (Fig. 15A).

Similar to changes in $R_N$, change in $\Delta n$ also begins near the ONH, as seen for four of five grade A2 $\Delta n$ profiles (Fig. 11B). Unlike $R_N$, however, $\Delta n$ profiles in all grade A1 and one grade A2 sector appeared normal, suggesting that $\Delta n$ is a less sensitive indicator of damage than short-wavelength change of $R_N$. With moderate cytoskeletal damage (grade A3) the $\Delta n$ profiles all fell below the normal range (Fig. 14B), with either a constant value (Fig. 13F) or with decreased $\Delta n$ near the ONH (Fig. 12B). Sectors with severe damage showed either decreased $\Delta n$ profiles or, unexpectedly, $\Delta n$ profiles within the normal range.

One explanation for normal $\Delta n$ profiles in sectors with overall severe cytoskeletal damage and RNFL thinning could be that the few surviving axons possess a cytoskeleton with an orderly array of nearly normal MTs. The flat spectra for the same sectors support the idea that the structures contributing to RNFL reflectance and birefringence are not the same and are consistent with studies that show MTs contribute differently to the two properties.[20,24] Indeed, the differing behavior of $R_N$ and $\Delta n$ for all grades of damage severity lends support to this idea.

Change of RNFL reflectance was not uniform across wavelengths; instead $R_N$ at short wavelengths responded earlier to structural damage. This may support the previously suggested two-mechanism model for the reflectance spectrum and also may provide a means to detect early damage in a clinical setting.[7] For example, RNFL spectra may be amenable to measurement by hyperspectral imaging,[37,38] or a ratio of short-to-long wavelength reflectance may capture the early change. In developing a spectral method, however, care will be required to account for short-wavelength absorption in the ocular media.

An advantage of using spectral shape is that it is not sensitive to the measurement geometry as long as the ranges of incident and scattering angles are restricted (Figs. 3B, 4B), as they are likely to be in clinical practice. This contrasts with the use of intrinsic reflectance, the internal RNFL reflectance seen on OCT, which several studies showed might provide sensitive detection of RNFL damage.[8–10,12] The measured value of RNFL reflectance is strongly affected by directional reflectance, as shown in Figure 3A and our earlier studies.[7,13] Clinical imaging systems do not simultaneously view all bundles at on-peak reflectance due to the change of bundle orientation around the ONH, introducing substantial variation into measurements of intrinsic reflectance.[13,39]

Although not as sensitive to early damage as $R_N$, measurements of the $\Delta n$ profile may provide an alternative method to detect early structural change in the RNFL. Birefringence is neither wavelength nor directionally dependent. As in the rat, nerve fiber bundles in normal human RNFL have constant $\Delta n$ profiles.[17–19] Whether they suffer early decline near the ONH in glaucoma remains to be determined, but further work is clearly desirable. Because birefringence and reflectance appear to depend differently on axonal cytostructure, the two approaches may even be complementary.

The rat model of glaucoma used in this study caused an acutely high IOP after laser treatment that then slowly decreased over time (Supplementary Fig. S3). Despite IOP as high as 56 mm Hg (the highest IOP observed in rat 6), the value was below the mean blood pressure of the normal rat (reported as approximately 70 mm Hg measured under anesthesia),[40] so a short exposure to the acutely high IOP is not expected to cause ischemic damage to the retina. We believe that the cytostructural distortion observed in this study

was caused by the moderate levels of IOP elevation over 2 weeks; that is, axonal damage due to prolonged IOP elevation. Also, the wide variation in damage observed across individual retinas argues against overall ischemia. Further, the tendency for changes to occur nearer the ONH in the less severely damaged sectors suggests that the ONH is the locus of the IOP insult. These characteristics of the rat model share similarity with human glaucoma and, hence, the findings obtained in this study may provide guidance for future studies of the relationship between changes of RNFL optical properties and ultrastructure in human glaucoma.

## References

1. Quigley H, Miller NR, George T. Clinical evaluation of nerve fiber layer atrophy as an indicator of glaucomatous optic nerve damage. _Arch Ophthalmol_. 1980;98:1564–1571.

2. Quigley HA, Katz J, Derick RJ, Gilbert D, Sommer A. An evaluation of optic disc and nerve fiber layer examinations in monitoring progression of early glaucoma damage. _Ophthalmology_. 1992;99:19–28.

3. Huang D, Swanson EA, Lin CP, et al. Optical coherence tomography. _Science_. 1991;254:1178–1181.

4. Knighton RW, Baverez C, Bhattacharya A. The directional reflectance of the retinal nerve fiber layer of the toad. _Invest Ophthalmol Vis Sci_. 1992;33:2603–2611.

5. Knighton RW, Zhou Q. The relation between reflectance and thickness of the retinal nerve fiber layer. _J Glaucoma_. 1995;4: 117–123.

6. Zhou Q, Knighton RW. Light scattering and form birefringence of parallel cylindrical arrays that represent cellular organelles of the retinal nerve fiber layer. _Appl Opt_. 1997;36: 2273–2285.

7. Knighton RW, Huang X-R. Directional and spectral reflectance of the rat retinal nerve fiber layer. _Invest Ophthalmol Vis Sci_. 1999;40:639–647.

8. Pons ME, Ishikawa H, Gürses-Özden R, Liebmann JM, Dou H, Ritch R. Assessment of retinal nerve fiber layer internal reflectivity in eyes with and without glaucoma using optical coherence tomography. _Arch Ophthalmol_. 2000;118:1044–1047.

9. Huang X-R, Zhou Y, Kong W, Knighton RW. Reflectance decreases before thickness changes in the retinal nerve fiber layer in glaucomatous retinas. _Invest Ophthalmol Vis Sci_. 2011;52:6737–6742.

10. van der Schoot J, Vermeer KA, de Boer JF, Lemij HG. The effect of glaucoma on the optical attenuation coefficient of the retinal nerve fiber layer in spectral domain optical coherence tomography images. _Invest Ophthalmol Vis Sci_. 2012;53:2424–2430.

11. Vermeer KA, van der Schoot J, Lemij HG, de Boer JF. RPE-normalized RNFL attenuation coefficient maps derived from volumetric OCT imaging for glaucoma assessment. _Invest Ophthalmol Vis Sci_. 2012;53:6102–6108.

12. Liu S, Wang B, Yin B, et al. Retinal nerve fiber layer reflectance for early glaucoma diagnosis. _J Glaucoma_. 2014; 23:e45–e52.

13. Huang X-R, Knighton RW, Feuer WJ, Qiao J. Retinal nerve fiber layer reflectometry must consider directional reflectance. *Biomed Opt Express*. 2016;7:22–33.

14. Huang X-R, Zhou Y, Knighton RW, Kong W, Feuer WJ. Wavelength-dependent change of retinal nerve fiber layer reflectance in glaucomatous retinas. *Invest Ophthalmol Vis Sci*. 2012;53:5869–5876.

15. Hemenger RP. Birefringence of a medium of tenuous parallel cylinders. *Appl Opt*. 1989;28:4030–4034.

16. Huang X-R, Knighton RW. Linear birefringence of the retinal nerve fiber layer measured in vitro with a multispectral imaging micropolarimeter. *J Biomed Opt*. 2002;7:199–204.

17. Cense B, Chen TC, Park BH, Pierce MC, De Boer JF. Thickness and birefringence of healthy retinal nerve fiber layer tissue measured with polarization sensitive optical coherence tomography. *Invest Ophthalmol Vis Sci*. 2004;45:2606–2612.

18. Huang X-R, Bagga H, Greenfield DS, Knighton RW. Variation of peripapillary retinal nerve fiber layer birefringence in normal human subjects. *Invest Ophthalmol Vis Sci*. 2004;45:3073–3080.

19. Sugita M, Pircher M, Zotter S, et al. Retinal nerve fiber bundle tracing and analysis in human eye by polarization sensitive OCT. *Biomed Opt Express*. 2015;6:1030–1054.

20. Huang X-R, Knighton RW. Microtubules contribute to the birefringence of the retinal nerve fiber layer. *Invest Ophthalmol Vis Sci*. 2005;46:4588–4593.

21. Fortune B, Wang L, Cull G, Cioffi GA. Intravitreal colchicine causes decreased RNFL birefringence without altering RNFL thickness. *Invest Ophthalmol Vis Sci*. 2008;49:255–261.

22. Pocock GM, Aranibar RG, Kemp NJ, Specht CS, Markey MK, Rylander HG. The relationship between retinal ganglion cell axon constituents and retinal nerve fiber layer birefringence in the primate. *Invest Ophthalmol Vis Sci*. 2009;50:5238–5246.

23. Knighton RW, Huang X-R, Zhou Q. Microtubule contribution to the reflectance of the retinal nerve fiber layer. *Invest Ophthalmol Vis Sci*. 1998;39:189–193.

24. Huang X-R, Knighton RW, Cavuoto LN. Microtubule contribution to the reflectance of the retinal nerve fiber layer. *Invest Ophthalmol Vis Sci*. 2006;47:5363–5367.

25. Weber A, Kaufman P, Hubbard W. Morphology of single ganglion cells in the glaucomatous primate retina. *Invest Ophthalmol Vis Sci*. 1998;39:2304–2320.

26. Shou T, Liu J, Wang W, Zhou Y, Zhao K. Differential dendritic shrinkage of α and β retinal ganglion cells in cats with chronic glaucoma. *Invest Ophthalmol Vis Sci*. 2003;44:3005–3010.

27. Taniguchi T, Shimazawa M, Hara H. Alterations in neurofilament light in optic nerve in rat kainate and monkey ocular hypertension models. *Brain Res*. 2004;1013:241–248.

28. Balaratnasingam C, Morgan WH, Bass L, Matich G, Cringle SJ, Yu D. Axonal transport and cytoskeletal changes in the laminar regions after elevated intraocular pressure. *Invest Ophthalmol Vis Sci*. 2007;48:3632–3644.

29. Balaratnasingam C, Morgan WH, Bass L, Cringle SJ, Yu D-Y. Time-dependent effects of elevated intraocular pressure on optic nerve head axonal transport and cytoskeleton proteins. *Invest Ophthalmol Vis Sci*. 2008;49:986–999.

30. Buckingham BP, Inman DM, Lambert W, et al. Progressive ganglion cell degeneration precedes neuronal loss in a mouse model of glaucoma. *J Neurosci*. 2008;28:2735–2744.

31. Huang X-R, Knighton RW. Altered F-actin distribution in retinal nerve fiber layer of a rat model of glaucoma. *Exp Eye Res*. 2009;88:1107–1114.

32. Salinas-Navarro M, Alarcon-Martinez L, Valiente-Soriano RJ, et al. Functional and morphological effects of laser-induced ocular hypertension in retinas of adult albino swiss mice. *Mol Vis*. 2009;15:2578–2598.

33. Fu CT, Sretavan D. Laser-induced ocular hypertension in albino CD-1 mice. *Invest Ophthalmol Vis Sci*. 2010;51:980–990.

34. Huang X-R, Kong W, Zhou Y, Gregori G. Distortion of axonal cytoskeleton: an early sign of glaucomatous damage. *Invest Ophthalmol Vis Sci*. 2011;52:2879–2888.

35. Knighton RW, Huang X-R. Visible and near-infrared imaging of the nerve fiber layer of the isolated rat retina. *J Glaucoma*. 1999;8:31–37.

36. Glovinsky Y, Quigley HA, Dunkelberger GR. Retinal ganglion cell loss is size dependent in experimental glaucoma. *Invest Ophthalmol Vis Sci*. 1991;32:484–491.

37. Harvey AR, Lawlor J, McNaught AI, Williams JW, Fletcher-Holmes DW. Hyperspectral imaging for the detection of retinal disease. *Proc SPIE*. 2002;4816:325–335.

38. Mordant DJ, Al-Abboud I, Muyo G, et al. Spectral imaging of the retina. *Eye*. 2011;25:309–320.

39. Knighton RW, Qian C. An optical model of the human retinal nerve fiber layer: implications of directional reflectance for variability of clinical measurements. *J Glaucoma*. 2000;9:56–62.

40. Levkovitch-Verbin H, Quigley HA, Martin KRG, Valenta D, Baumrind LA, Pease ME. Translimbal laser photocoagulation to the trabecular meshwork as a model of glaucoma in rats. *Invest Ophthalmol Vis Sci*. 2002;43:402–410.

Investigative Ophthalmology & Visual Science